High Resolution Magnetotelluric Imaging of the Nisyros Caldera and Geothermal Resource (Greece)

Andreas Tzanis[1], Vassilis Sakkas[2] and Evangelos Lagios[3]

Section of Geophysics and Geothermy, National and Kapodistrian University of Athens

[1]*atzanis@geol.uoa.gr*; [2]*vsakkas@geol.uoa.gr*; [3]*lagios@geol.uoa.gr*

1. Tectonics and the Geothermal Resource

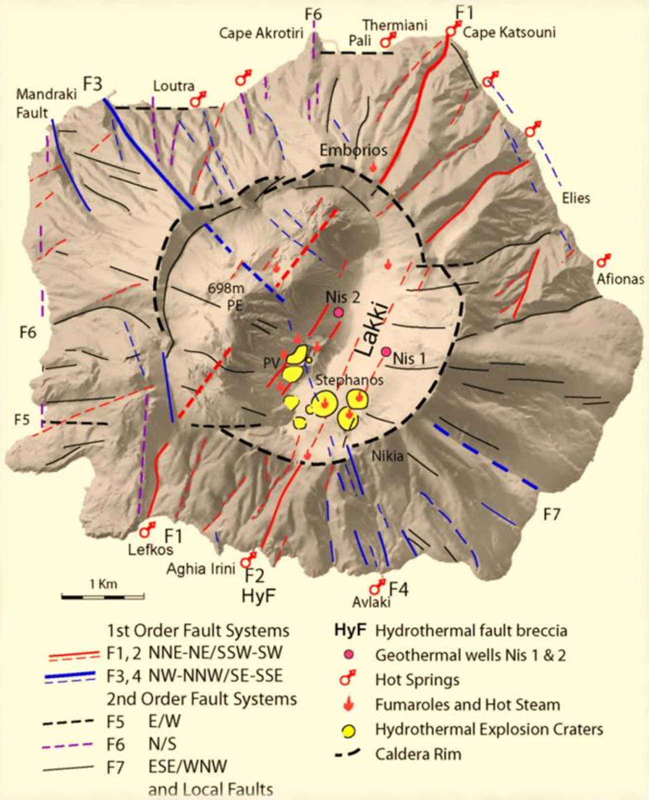

- Active Quaternary calc-alcaline volcano.
- Caldera formed ca. 44-24 Ka BCE
- NE half of caldera partially filled with rhyolitic – dacitic extrusives ca. 24 Ka BCE.
- High temperature (> 300°C) hydrothermal resource with intense fumarolic activity developed in SW half of caldera (Lakki).
- 1422 – 1888 CE: Phreatic explosion craters formed during extended episodic activity. Stephanos crater formed in 1873 CE.
- Hydrothermal circulation apparently controlled by ***first order*** active faulting
- F1 : Forms NW flank of Lakki; Strike N30°; Dip direction N120°; Dip 70°-80°; Throw ~100m.
- F2 : Forms SE flank of Lakki; Strike N30°; Dip direction N300°; Dip 70°-80°; Throw 100 – 120m.
- F3 : Appears mainly in NE sector of island; Strike N320°-330°; Dip direction N50°-60°; Dip 70°-80°; Throw > 100m.
- F4 : Appears in SSW sector of island and forms narrow graben-like depression; Strike N340°; Dip 70°-80°.
- F1, F2 and F4 fault zones associated with underwater thermal springs at intersections with coastline

2. Data Acquisition & Processing

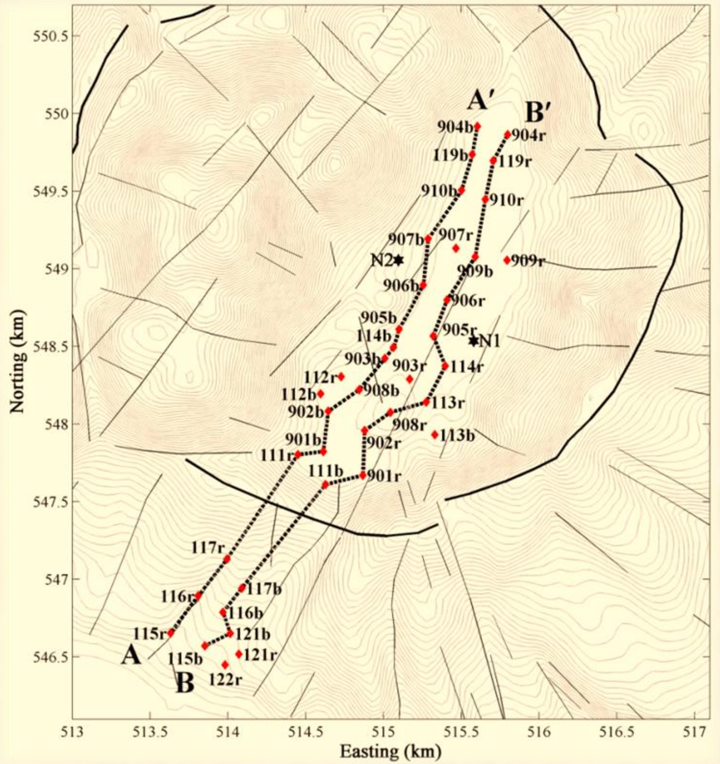

Location of the 39 MT stations. N1 and N2 are the deep exploration wells. AA′ and BB′ are the Transects along which 2-D inversion was carried out.

- Legacy Data: SPAM MkIIb system (Dawes 1984); bandwidth 128Hz-40s; $Pb/PbCl_2$ electrodes; CM11 induction coils.

- 39 soundings conducted in the Magnetotelluric – Telluric configuration with one 5-component *Base* MT station and one 2-component *Remote* Telluric station at a time.
  - ➢ xxxB : Base Station
  - ➢ xxxR : Remote Station

- Impedance Tensor elements are estimated in two steps:
  - ➢ First step: Standard single-site processing techniques (Sims et al., 1971).
  - ➢ Second step: Spectral components E_x, E_y, H_x, H_y yielding impedance tensor realizations with predicted coherence > 0.8 were used in a robust procedure similar to that of Egbert and Booker (1986)

- Similar procedure used to estimate Magnetic Transfer Functions (hence Induction Vectors).

3. Tensor Decomposition

- We implement an anti-symmetric reformulation of the *equivalent* Canonical (Yee & Paulson, 1987) and Singular Value (LaToracca et al, 1986) decompositions of the impedance tensor developed by Tzanis (2014). The decomposition reads:

$$\mathbf{Z} = \mathbf{U}(\theta_E, \Phi_E) \cdot \begin{bmatrix} 0 & \zeta_1 \\ -\zeta_2 & 0 \end{bmatrix} \cdot \mathbf{V}^\dagger(\theta_H, \Phi_H)$$

- where **U** and **V** are SU(2) matrices, of the form $\mathbf{U}(\theta,\Phi) = \begin{bmatrix} \cos\theta\cos\Phi - i\sin\theta\sin\Phi & -\cos\theta\sin\Phi + i\sin\theta\cos\Phi \\ \cos\theta\sin\Phi + i\sin\theta\cos\Phi & \cos\theta\cos\Phi + i\sin\theta\sin\Phi \end{bmatrix}$

- At any location on the surface of the Earth, the impedance tensor can be re-written as

$$\mathbf{U}^\dagger\mathbf{Z} = \begin{bmatrix} 0 & \zeta_1 \\ -\zeta_2 & 0 \end{bmatrix} \cdot \mathbf{V}^\dagger \Rightarrow \begin{bmatrix} E_1(\theta_E, \Phi_E) \\ E_2(\theta_E, \Phi_E + \frac{\pi}{2}) \end{bmatrix} = \begin{bmatrix} 0 & \zeta_1 \\ -\zeta_2 & 0 \end{bmatrix} \cdot \begin{bmatrix} H_1(\theta_H, \Phi_H) \\ H_2(\theta_H, \Phi_H + \frac{\pi}{2}) \end{bmatrix}$$

  - $\{E_1(\theta_E, \Phi_E), H_2(\theta_H, \Phi_H)\}$ is the ***maximum characteristic state*** (***generalized eigenstate***) of the EM field
  - $\{E_2(\theta_E, \Phi_E+\pi/2), H_1(\theta_H, \Phi_H+\pi/2)\}$ is the ***minimum characteristic state*** of the EM field.

- The angles (θ_E, Φ_E) define a ***characteristic coordinate frame*** or ***eigen-frame*** $\{x_E, y_{E,}, z_E\}$ of the E-field, such that x_E is rotated by Φ_E clockwise with respect to the *x*-axis of the experimental coordinate frame and the plane $\{x_E, y_E\}$ is tilted by an angle θ_E clockwise with respect to the horizontal plane $\{x, y\}$.
- The angles (θ_H, Φ_H) define the corresponding *eigen-frame* $\{x_H, y_{H,}, z_H\}$ of the H-field.
- Generally, $\Phi_E \neq \Phi_H$ and/or $\theta_E \neq \theta_H \neq 0$; for 2-D geoelectric structures, $\Phi_E = \Phi_H$ and $\theta_E = \theta_H \rightarrow 0$.
- The *projection* of an eigenstate on the ***horizontal plane*** comprises ***elliptically polarized*** components; the ***ellipticity***, given by $b = \tan\theta$, is defined in terms of a ***rotation*** in higher dimensional space!

4. Typical Impedance Tensors

Sounding 908B:

- Weak 3-D effects at short periods, evident in the maximum/minimum apparent resistivities and phases (**A** and **B**) and the skewness of the electric and magnetic eigen-frames in (**C**) where $\Phi_E \neq \Phi_H$.
- Moderate 3-D effects at longer periods as seen in the skewness & variability of Φ_E, Φ_H in (**C**) and the non-trivial tilt of the eigen-frames in (**D**).

Sounding 111B:

- For periods up to 1s, 2-D characteristics evident in all parameters of the maximum and minimum eigen-frames because $\Phi_E \approx \Phi_H$ and $\theta_E \approx \theta_H \approx 0$ (trivial tilts).
- Very weak 3-D structural attributes appear at periods longer than 10s.

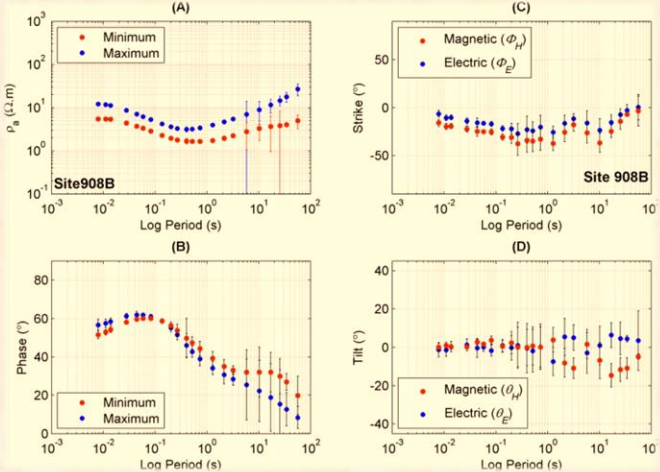

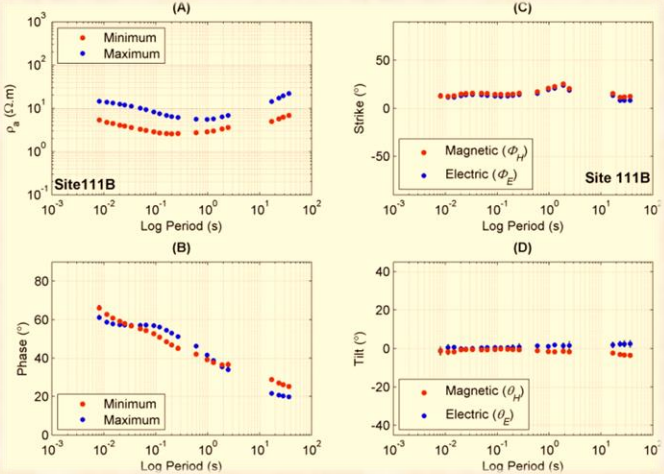

5. Configuration of the Electric Structure

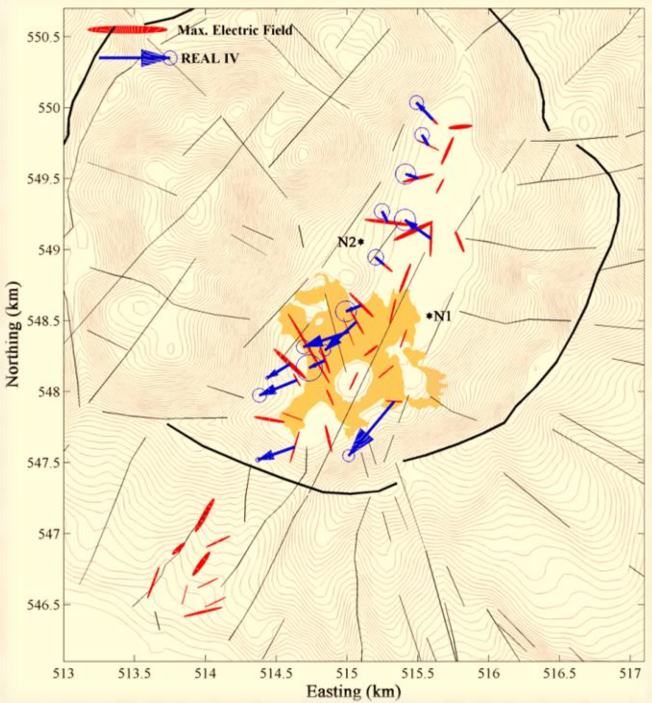

Max. Electric Polarization state (E_{max}) and Real Induction Vectors mapped as averages over 2–100s. Orange shaded area: Debris flow and deposits related to the 1873 CE activity.

- The mutual configuration of electric polarization ellipses and real induction vectors indicates:
- Inside the caldera (Lakki), in the area of the 1873 CE hydrothermal activity:
  - E_{max} polarization ellipses are NNW-SSW oriented, ***orthogonal*** to SSW pointing Real Induction Vectors
  - Configuration consistent with **TE induction over a NNW-SSE 2-D conductive dyke** – presumably the graben formed by the F4 fault zone
- At the SW terminus of Lakki and along its west flank northward of the 1873 CE hydrothermal activity:
  - E_{max} polarization ellipses are W-E to NW-SE and of ***comparable orientation*** to the Real Induction vectors.
  - Configuration consistent with **TM induction above the resistive side of a NNE-SSW conductivity interface**.
- Almost everywhere else (outside the caldera and inside the caldera along the BB′ Transect northwards of Stephanos crater) the orientations of E_{max} polarization ellipses are NNE-SSW and consistent with **TE induction over a NNE-SSW conductive dyke** presumed to be associated with the F2 fault zone.

6. Regional Geoelectric Strike

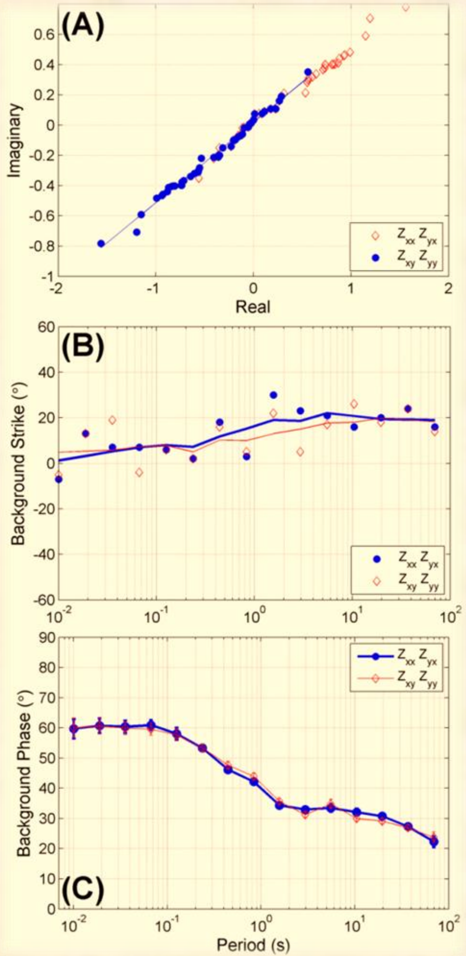

- In a regional 2-D structure, impedance tensor elements of the same column vector can be regarded as electric fields produced by a magnetic field parallel or perpendicular to the regional strike
- Banks and Wright (1998): the presence of a regional 2D structure is manifest in the common phase of tensor elements belonging to the same column.
  - **Fig A:** The real and imaginary parts of E-fields rotated to the direction of the regional response will plot on a line of constant phase in the complex plane.
- **Fig B: Background strike is:**
  - Rather unstable if not erratic at short periods, where it exhibits an N-S average orientation
  - Rather stable at periods > 1s, where it indicates a N20° orientation *consistent* with the strike of F1 and F2 and Lakki.
- By association with Transparency 5, it is clear that in the south half of Lakki, Fault Zone F4 is locally dominating EM induction and comprises a major component of hydrothermal activity.
- **Fig. C: The regional phase** indicates *two* background structures:
  - One shallow, very conductive, evident at periods < 0.2s, presumably associated with the hydrothermal field.
  - One deep, relatively resistive, evident at periods > 1s and presumably associated with the deeper structure of the volcano's.

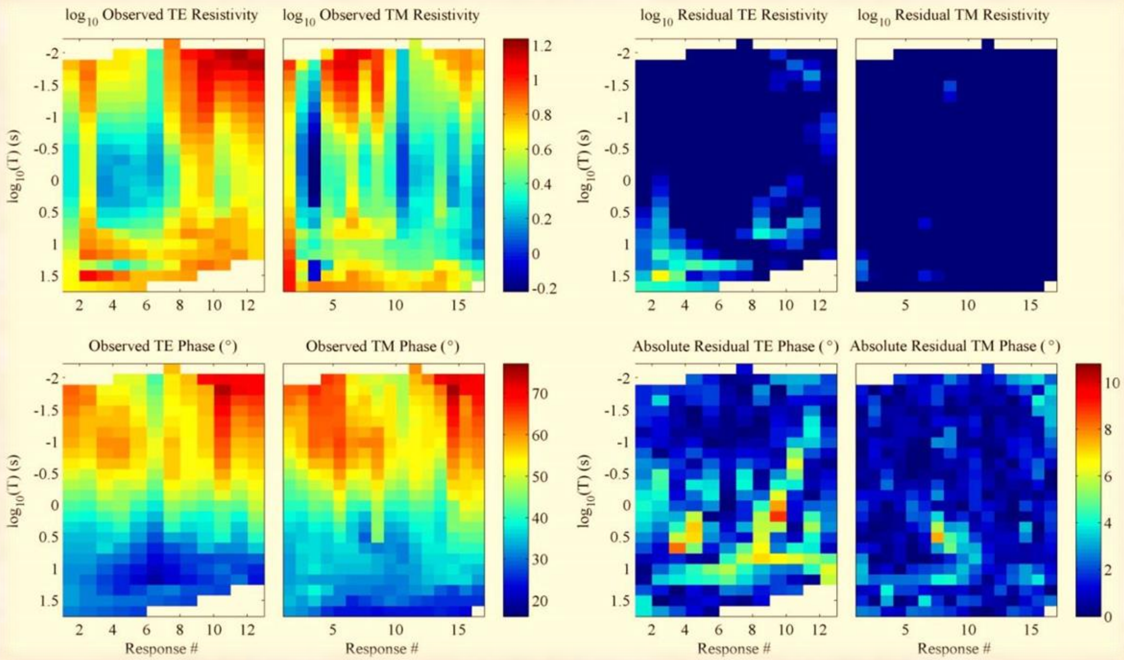

7. Two-Dimensional Inversion after Rodi and Mackie (2001)

- TE and TM modes simultaneously inverted along transects AA′ and BB′ using spatial configuration described above.
- West Transect: Final χ^2 misfit 1357; Expected χ^2 misfit 952; Higher than expected χ^2 attributed to the moderate local 3-D effects: Overall successful reconstruction of resistivity structure.
- East Transect: Final χ^2 misfit 1781; Expected χ^2 misfit 976; Comments as per West Transect above.
- Example shown: Observed (left) and residual (right) TE and TM apparent resistivity and phase responses along the East Transect (BB′). In each panel, every column corresponds to one sounding curve and the order of columns corresponds to the order of soundings along the transect.

8a. Resistivity Structure I: Correlation with Boreholes

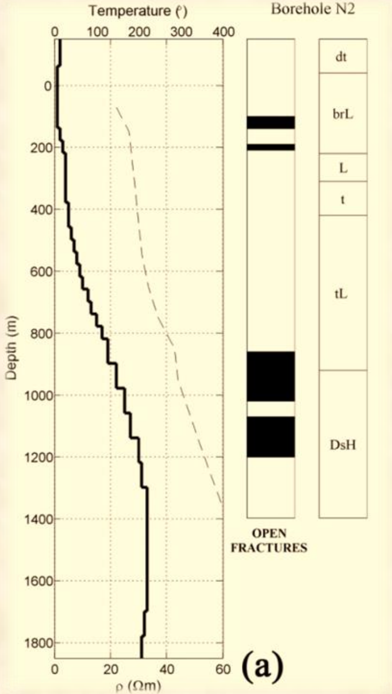

- Fractures/high permeability in **BLACK SHADING**
- Lithological abbreviations: **dt** detritus; **brL** brecciated lava; **L** lava; **t** tuff; **tL** tuff and lava; **DsH** dioritic subintrusives and hornhels.
- Information from Ungemach (1983), Geotermica Italiana (1983).

N2 vs. West Transect (A-A′)

1. 20–200m BSL: 1Ωm conductor in the argillic alteration zone + intense hydrothermal activity indicates shallow reservoir + extensive argillization.
2. 100-210m BSL: Fractures due to F1, F3 + high permeability; water bearing formation between 150-300m BSL corresponds to 2–4 Ωm conductor between 150–400m overlapping with fractured zone.

- Interpretation: Fragmentation generates circulation zone feeding “shallow reservoir” in the argillic alteration zone (1 Ωm conductor) + circulation zone and deeper reservoir in the phyllic alteration zone (2–4 Ωm conductor).

3. Gradual increase in temperature between 200-900m is attributed to low permeability + apparent absence of sea water infiltration and corresponds to gradual increase in resistivity to > 20Ωm by corresponding decrease of volumetric content in hydrophile clay minerals in the phyllic alteration zone.
4. Permeability due to fracturing is high at depths 900m-1200m BSL (cause not identified) and remains significant up to 1400. Exceptional conductor is not detected but resistivity increase is halted after 1300m and reversed after 1700m: behaviour consistent with deep circulation zone and reservoir in a domain free of sea water infiltration.

8b. Resistivity Structure I: Correlation with Boreholes

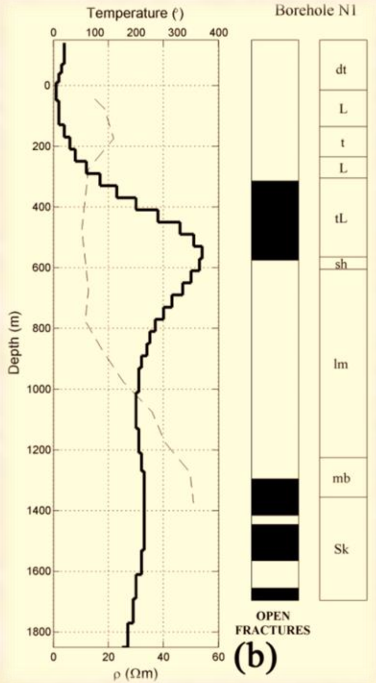

- Fractures/ high permeability shown in **BLACK SHADING**.
- Lithological abbreviations: **dt** detritus; **L** lava; **t** tuff; **tL** tuff and lava; **sh** shales; **lm** limestone; **mb** marble; **Sk** skarn.
- Information from Ungemach (1983). Geotermica Italiana (1983).

N1 vs. East Transect (B-B′)

1. Very good 1-2Ωm conductor at *sea level* corresponds to caldera infill altered in the argillic alteration zone: combination of high fractional content in hydrophile clay minerals + electrolytes.
2. At depths 160-200m the temperature exhibits local peak (150°C) coinciding with argillic-phyllic transition due to *shallow reservoir*; resistivity increases to 6-8 Ωm by reduction of hydrophile clay mineral content in the phyllic alteration zone.
3. Depths 300-600m: Temperature drops to 70–90° in coincidence highly permeable domain at 310–600m, attributed to F2 and the caldera wall – indicates infiltration of seawater through F4 and F2. The resistivity increases locally to approx. 54 Ωm at the depth of 600m both due to reduction in temperature in the phyllic zone and, possibly, the same dioritic intrusion as per N2.
4. Depths > 400m – 600m: *Resistivity profile does not correspond to the lithological column at N1* because the former represents formations located within the caldera and while the latter is outside of the. Resistivity decrease to ~30 Ωm at depths > 900m (comparable to that observed near N2) indicates possibility of deep circulation at 1300–1800m.

9. Resistivity Structure I: West Transect (A-A′)

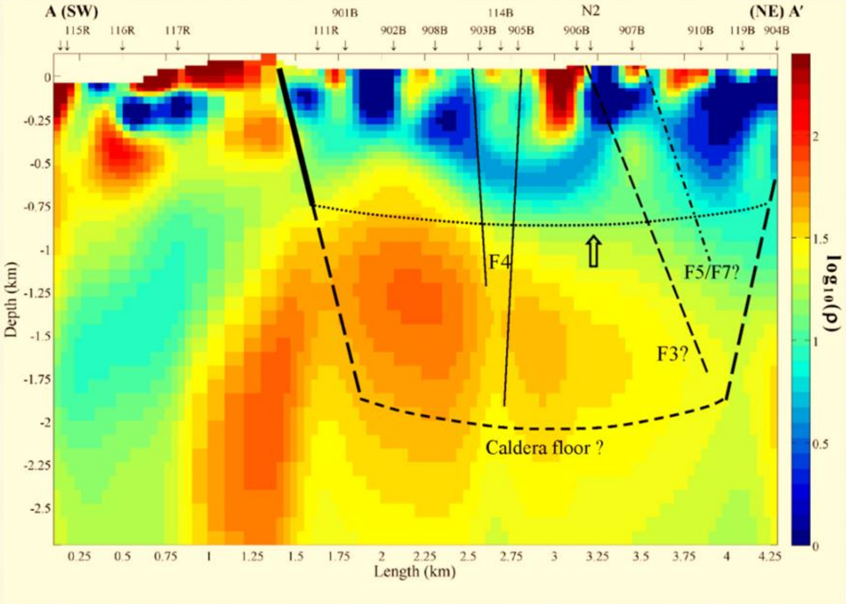

2-D best-fitting model of resistivity structure along the West Transect A-A′. N2 marks the nearest to well N2 location of the Transect. The up-arrow points to the inferred ceiling of the dioritic intrusion at N2.

- The southern boundary fault of caldera is clearly resolved.
  - At depths > 1 km it is seen as conductive dent in a relatively resistive formation
- The location of the northern boundary fault is conjectured by the relative conductive dent at depths > 1.25 km.
- Resistive formation at depths 0.8–2.5 Km attributed to >24 Ka dioritic intrusion found by drilling.
- Horizontal dotted line marks approximate depth extent of geothermal system (interconnected network of reservoirs and circulation zones).
  - Good conductors up to 0.25 Km represent the combined effect of clay mineralization and fluid concentration in the ***argillic*** hydrothermal zone.
  - **Deeper (0.25–0.8 Km) conductors** likely represent fluid concentration and circulation in the ***phyllic*** hydrothermal zone.
- Conductors that are apparently associated with faulting indicate deep circulation zones.
- Lines marked F4 connect trace of homonymous faults through a dent in the resistivity of dioritic intrusion to good conductor at depths >2 Km. The conductive dent is interpreted to be **epiphenomenal effect** of the permeable fault zone.

10. Resistivity Structure II: East Transect (B-B′)

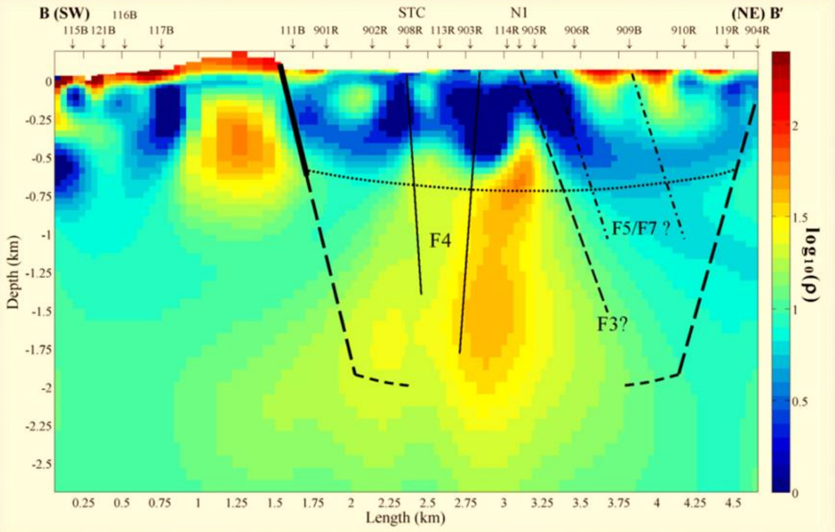

2-D best-fitting model of resistivity structure along the East Transect B-B′. STC marks the position of Stephanos phreatic explosion crater. N1 marks the nearest to well N1 location of the Transect.

- At depths < 0.6 Km the structure is definitely more conductive than in A-A′. Since B-B′ literally sits on the F2 zone the effect is attributed to fluid circulation and diffusion associated with this fault zone.
- The southern boundary fault of caldera is clearly resolved at depths < 0.8 Km but cannot be readily traced to larger depths.
- The northern boundary fault cannot be observed and is indicated by conjecture
- The relative resistor at depths 0.6–2.3 Km is attributed to country rock and the >24 Ka dioritic intrusion, as per A-A′.
- Horizontal dotted line marks approximate extent of geothermal system as per A-A′.
- Conductors that are apparently associated with faulting indicate deep circulation zones (e.g. F3, F5).
- Lines marked F4 connect trace of homonymous fault through a good sub-vertical conductor and a low-resistivity dent in the dioritic intrusion to a good conductor at depths >2Km. The low-resistivity dent is interpreted as per A-A′.

11. Conclusions

- ✓ The structure comprises a quasi-2D, low-contrast background defined by the first order faulting systems, decorated by local, low-contrast 3-D inhomogeneities.
- ✓ Low contrasts may results from the smoothing effect of intense tectonic/ hydrothermal activity with associated extensive fluid diffusion and pervasive alteration.
- ✓ Very shallow (0.1-0.3 Km) resistivity structure characterized by interconnected conductive enclosures (<2Ωm) corresponding to fluid concentrations (reservoirs) within the ***argillic alteration zone***.
- ✓ Between 0.3–1 Km these merge into extended low resistivity (<12 Ωm) zones representing fluid concentrations and circulation in the ***phyllic*** and ***phyllic-propylitic*** alteration zones.
- ✓ The development of reservoirs and the lateral circulation and diffusion of fluids at all depths is facilitated by faulting, often resulting in the formation of fault-aligned epiphenomenal conductors.
- ✓ The deep (>1 Km) convection and circulation zones are generally associated with major normal faults and their intersection, with particular reference to the NE-SW F1/F2 system and the NNW-SSE F4 zone (particularly active at the SW sector of the island; defines the main convection path).
- ✓ Between 1–2 Km, fault-aligned convection paths associated with F4 is imaged as sub-vertical low-resistivity dents in the (relatively) resistive signature of presumed dioritic intrusions.
- ✓ Results and conclusions are still approximate: local (weak) 3-D effects could not be fully resolved and the fine detail of the resistivity structure would not be assessed.

12. References

- Banks, R.J. and Wright, D., 1998. Telluric analysis of distributed magnetotelluric impedance measurements, *Annales Geophys.*, *Suppl. 1 to v16*, C275; presented in XXIII EGS Gen. Assembly, Nice, France, 20-24 April 1998.
- Dawes, G.J.K., 1984. Short Period Automatic Magnetotelluric (S.P.A.M.) system. In: A Broadband Tensorial Magnetotelluric Study in the Travale-Radicondoli Geothermal Field. EC Final Report, Contract No. EG-A2-031-UK.
- Egbert, G.D. and Booker, J.R., 1986. Robust Estimation of Geomagnetic Transfer Function Data, *Geophys. J. R. astr. Soc.*, 87, 173-194.
- Geotermica Italiana, Srl, 1983. Nisyros-1 geothermal well. Final report, submitted to PPC/DEME.
- LaTorraca, G., Madden, T. and Korringa, J., 1986. An analysis of the magnetotelluric impedance tensor for three-dimensional structures, *Geophysics*, 51, 1819–1829.
- Sims, W.S., Bostick, F.X., Jr. and Smith, H.W., 1971. The estimation of magnetotelluric impedance tensor elements from measured data, *Geophysics*, 36, 938-942.
- Tzanis, A., 2014. The Characteristic States of the Magnetotelluric Impedance Tensor: Construction, analytic properties and utility in the analysis of general Earth conductivity distributions, arXiv:1404.1478 [physics.geo-ph]; last accessed, July 15, 2015.
- Ungemach, P., 1983. Nissyros Geothermal Wildcut Drilling, Testing, Sampling, 6 June 3 December 1982, Exec. Summary, Preliminary report, EEC Contract No EG-A-1-046-G and EG-A-Y-113-I.
- Yee, E., and Paulson, K.V., 1987. The canonical decomposition and its relationship to other forms of magnetotelluric impedance tensor analysis, *J. Geophys.*, 61, 173–189.